RESEARCH ARTICLE | DECEMBER 04 2025

A full-field noise conversion model of different Mach numbers for flows past a cylinder at Reynolds number 3900

Jiajia Qin (秦佳佳) ; Haiting Yu (余海廷); Decheng Wan (万德成) ; Yuan Zhuang (庄园)

Physics of Fluids 37, 125122 (2025)
https://doi.org/10.1063/5.0302360

Physics of Fluids ARTICLE pubs.aip.org/aip/pof

A full-field noise conversion model of different Mach numbers for flows past a cylinder at Reynolds number 3900

Cite as: Phys. Fluids **37**, 125122 (2025); doi: 10.1063/5.0302360
Submitted: 15 September 2025 · Accepted: 14 November 2025 ·
Published Online: 4 December 2025

Jiajia Qin (秦佳佳),[1] Haiting Yu (余海廷),[2] Decheng Wan (万德成),[1] and Yuan Zhuang (庄园)[1,a)]

AFFILIATIONS

[1]Computational Marine Hydrodynamic Lab (CMHL), School of Ocean and Civil Engineering, Shanghai Jiao Tong University, Shanghai 200240, China
[2]Wuhan Second Ship Design and Research Institute, Wuhan, China

[a)]Author to whom correspondence should be addressed: nana2_0@sjtu.edu.cn

ABSTRACT

For the benchmark simulation of flow past a stationary body, dipole source constitutes the principal noise-generating mechanisms. However, in underwater environments, the extremely low signal-to-noise ratio (SNR) renders experimental noise measurements particularly challenging, making it quite difficult to obtain accurate results. To address this limitation, the present study employs the noise conversion exponents *Na* and *Nu*, thereby extending existing noise conversion methodologies of different Mach numbers for noise conversion between two different media. These exponents are applied to enable mutual conversion between low-Mach-number aerodynamic noise and hydrodynamic noise at identical Reynolds numbers, allowing high-SNR aerodynamic acoustic experimental data to be leveraged for more reliable hydrodynamic noise prediction. In this work, the open-source solver OpenFOAM is employed to simulate flow past a circular cylinder, and dynamic mode decomposition in conjunction with wavelet analysis is utilized to perform both qualitative and quantitative investigations of hydrodynamic and aerodynamic flow-induced noise. The similarities and differences between the two cases are examined in detail in both the flow field and the acoustic field. The noise conversion exponents *Na* and *Nu* are then applied to achieve effective cross-domain noise conversion. Results indicate that, for observers with identical radii but different azimuthal positions, the *Nu* facilitates accurate conversion from aerodynamic noise to hydrodynamic noise, whereas for observers with identical azimuthal positions but different radii, the *Na* works. The proposed noise conversion exponents thus provide a valuable framework for predicting underwater noise from wind tunnel acoustic measurements.

I. INTRODUCTION

Flow-induced noise is prevalent in engineering fields such as aerospace, marine propulsion, and underwater vehicles, acting as a key factor affecting structural fatigue life and acoustic stealth performance.[1–3] As the demand for enhanced acoustic stealth in underwater equipment such as submarines continues to rise, accurate prediction and control of hydrodynamic noise become increasingly crucial. However, the unique characteristics of the underwater environment, such as high background noise, low compressibility of the medium, and complex sound propagation characteristics, pose significant challenges to high-precision experimental measurements of hydrodynamic noise.[4,5] Consequently, experimental results are limited, and existing studies predominantly rely on high-fidelity numerical simulations.

Compared with underwater noise measurements, aerodynamic noise testing in wind tunnels has reached a relatively mature stage,[6–8] encompassing well-established theoretical frameworks,[9–11] advanced numerical simulation methods,[12–14] and experimental measurement techniques.[15,16] According to the Ffowcs Williams–Hawkings (FW–H) equation,[17] the sound source terms are categorized into monopole, dipole, and quadrupole components. For a stationary object, there is no monopole sound source term. For the aeroacoustics field with a Mach number (*Ma*) lower than 0.2, quadrupole can usually be neglected. Nitzkorski and Mahesh[18] compared the results of direct numerical simulation (DNS) with those obtained from surface integrals accounting solely for dipole contributions and found strong agreement between them. Zheng[19] took the dipole sound sources as the actual sound sources to analyze the aerodynamic noise generated by tandem circular cylinders immersed in a three-dimensional turbulent flow. Good comparisons are obtained between numerical results and Basic Aerodynamic Research Tunnel (BART) experimental data

published by NASA. Furthermore, the directivity patterns presented in Refs. 20–22 displayed dipole-like characteristics, further confirming that in aerodynamic noise with low *Ma*, quadrupole contributions are relatively minor, with dipoles being the dominant source which are related to wall pressure fluctuation.[23–25]

Flow field similarity is governed by the Reynolds number (*Re*).[26] When *Re* is identical, the non-dimensional flow field statistics of hydrodynamic and low-Mach-number aerodynamic flows, which can be regarded as incompressible, are generally consistent. For instance, Fan *et al.*[27] compared numerical results of hydrodynamic flow past a cylinder at $Re = 3900$ with experimental results[28] of aerodynamic flow past a cylinder at the same *Re*, revealing agreement in key flow features such as lift and drag coefficients (C_l, C_d), Strouhal number (*St*), and wake velocity profiles. Liu *et al.*[29] compared hydrodynamic cylinder flow at $Re = 3900$ with aerodynamic numerical simulation,[30] and the result is also the same. While these investigations validated the consistency of time-averaged statistical quantities between aerodynamic and hydrodynamic flows at the same *Re*, they fell short of providing systematic comparative analyses of transient flow structures, such as vortex shedding and pressure fluctuation patterns for air and water with the same *Re*. Furthermore, the significant differences in density, viscosity, and sound propagation speed between water and air lead to a pronounced difference in Mach number even under similar flow conditions. This, in turn, leads to markedly distinct acoustic field characteristics, especially in the far field due to differing propagation and radiation mechanisms. Jacob and Bhattacharyya[31] compared hydrodynamic and aerodynamic cylinder flow at $Re = 19\,800$ and found that while hydrodynamic noise levels were higher, they decayed more rapidly with distance. The study by Poggi *et al.*[32] also confirmed the strong influence of the Mach number on noise radiation magnitude and directivity. This observation aligns with the Farassat 1A formulation[33] of the FW–H equation, which indicates that sound propagation is dependent on the local Mach number in the direction of propagation. As a result, although aerodynamic and hydrodynamic flows may exhibit similar flow fields, their acoustic characteristics, including radiation efficiency, directivity, and spectrum, can differ substantially.

In recent years, there exists some research in noise conversion for aerodynamic flows of different Mach numbers. The study of Jiang *et al.*[34] demonstrated that squared acoustic pressure scales approximately with the fifth power of the Mach number and shows minimal dependence on the observer's position. For thicker airfoils, this scaling law provides better sound predictions than flat plate theory. Turner and Kim[35] proposed noise conversion formulas for flows of different Mach numbers, with *Na* and *Nu* as conversion exponents based on different non-dimensional Strouhal numbers. However, their study was limited to comparisons at four specific observer angles for medium-Mach-number aerodynamic airfoils, without clearly defining the applicability conditions of the proposed exponents. Since aerodynamic and hydrodynamic noise essentially correspond to flows with different Mach numbers, and particularly because low-Mach aerodynamic flows can be regarded as incompressible, like hydrodynamic flows, the primary distinction lies in the Mach number itself. Theoretically, this suggests that conversion methods based on Mach number differences could be applicable to aerodynamic–hydrodynamic noise conversion. This paper extends prior efforts by clearly defining the application scenarios for *Na* and *Nu*, applying them to full-field noise observers, and achieving effective quantitative conversion between aerodynamic and hydrodynamic noise, offering a deeper exploration than studies limited to a few angles.

In this study, flow past a circular cylinder at $Re = 3900$ is simulated as the research subject. It is a well-established benchmark case in fluid dynamics and aeroacoustics, providing high-quality reference data for model validation. More importantly, the wake exhibits a fully formed von Kármán vortex street and strong fluctuating lift forces, resulting in dipole-dominated noise, which is exactly the physical condition relevant to our study. The geometric model remains identical in both aerodynamic and hydrodynamic flow simulations, with an aerodynamic Mach number of 0.2 and a hydrodynamic Mach number of 0.003. A high-fidelity three-dimensional transient numerical model is established based on the OpenFOAM open-source solver. The turbulence model is based on wall-modeled large eddy simulation (WMLES), coupled with a non-equilibrium ODE-based wall model (NEQWM) to accurately capture near-wall flow behavior. Dynamic mode decomposition (DMD) is employed for qualitative and quantitative analysis of dipole modes in both aerodynamic and hydrodynamic flows. The far-field noise is computed using the surface integral method of the FW-H acoustic analogy equation. Computational results are quantitatively compared, and wavelet decomposition is applied to investigate the propagation characteristics of aerodynamic and hydrodynamic noise. The noise conversion formulas for flows of different Mach numbers proposed by Turner and Kim[35] are extended to full-field cross-medium noise conversion in this paper, enabling the conversion between low-Mach-number hydrodynamic noise and incompressible-flow aerodynamic noise. This approach allows wind tunnel experimental results to be used for predicting hydrodynamic noise at the same *Re*.

Finally, the paper is organized as follows: Sec. II introduces the numerical methodology, including the NEQWM model for WMLES and the FW-H equation. Section III presents and analyzes the results in depth, covering the fundamental similarities and differences between aerodynamic and hydrodynamic noise in terms of flow field statistics, dipole sound sources, and acoustic field characteristics, and further explores the quantitative relationship between them. The final conclusions are drawn in Sec. IV.

II. NUMERICAL METHODOLOGY

A. Large eddy simulation

The fundamental concept of LES is to apply spatial filtering to the Navier–Stokes (N–S) equations using a filtering function. Large-scale turbulent fluctuations are resolved directly through numerical computation, while the effects of small-scale fluctuations on the large-scale motions are modeled using sub-grid-scale stress (SGS) models. After applying spatial filtering to the N–S equations, the governing equations suitable for LES can be obtained as follows:

$$\frac{\partial \tilde{u}_i}{\partial t} + \frac{\partial \tilde{u}_i \tilde{u}_j}{\partial x_j} = -\frac{1}{\rho}\frac{\partial \tilde{p}}{\partial x_i} + \nu \frac{\partial^2 \tilde{u}_i}{\partial x_j \partial x_j} - \frac{\partial \tau_{ij}}{\partial x_j}, \tag{1}$$

$$\frac{\partial \tilde{u}_i}{\partial x_i} = 0. \tag{2}$$

Here, $\tilde{u}_i$ denotes the velocity components after spatial filtering, with $i = 1, 2, 3$ corresponding to the x_1, x_2, and x_3 directions, respectively. $\tilde{p}$ is the pressure field after spatial filtering. ν represents the

kinematic viscosity of the fluid. τ_{ij} is the SGS tensor, which can be further expressed in the following form:

$$\tau_{ij} = \frac{2}{3}k_{sgs}\delta_{ij} - 2\nu_{sgs}\tilde{S}_{ij}, \tag{3}$$

where k_{sgs} is the SGS kinetic energy, $\tilde{S}_{ij}$ is the resolved strain-rate tensor, δ_{ij} is the Kronecker delta, and ν_{sgs} is the SGS eddy viscosity.

B. Wall stress model

Wall-resolved large eddy simulation (WRLES) requires extremely fine grid resolution within the boundary layer to accurately capture near-wall turbulence at high *Re*. In contrast, WMLES offers an effective solution by reducing computational cost while maintaining accuracy. In this study, a WMLES approach based on NEQWM is employed. The wall shear stress is expressed as follows:

$$\tau_{wi} = \mu\frac{\partial u_i}{\partial x_2}\bigg|_{x_2=0} = \frac{\rho}{\int_0^h \frac{dx_2}{\nu+\nu_\tau}}\left\{u_{h_i} - F_i\int_0^h \frac{x_2 dx_2}{\nu+\nu_\tau}\right\}, \tag{4}$$

$$F_i = \frac{1}{\rho}\frac{\partial p}{\partial x_i} + \frac{\partial u_i}{\partial t} + \frac{\partial}{\partial x_j}(u_i u_j). \tag{5}$$

Here, U_{h_i} denotes the sampled velocity at a distance h from the wall. According to the study by Fan *et al.*,[27] setting h = 2 provides a good simulation of the flow field.

C. FW-H equation

The acoustic analogy equation employs the FW-H equation, and the Farassat 1A formula is its commonly used integral form solution. The acoustic pressure is obtained by summing the thickness noise derived from the monopole term and the loading noise derived from the dipole term, as follows:

$$p_{T'} = \frac{1}{4\pi}\left(\int_{f=0}\left[\frac{\rho_\infty(\dot{U}_n + U_n)}{r(1-M_r)^2}\right]_{\text{ret}} dS + \int_{f=0}\left[\frac{\rho_\infty U_n\left(r\dot{M}_r + c_0(M_r - M^2)\right)}{r^2(1-M_r)^3}\right]_{\text{ret}} dS\right), \tag{6}$$

$$p_{L'} = \frac{1}{4\pi c_0}\left(\int_{f=0}\left[\frac{\dot{L}_r}{r(1-M_r)^2}\right]_{\text{ret}} dS + \int_{f=0}\left[\frac{c_0(L_r - L_M)}{r^2(1-M_r)^2}\right]_{\text{ret}} dS + \int_{f=0}\left[\frac{L_r\left(r\dot{M}_r + c_0(M_r - M^2)\right)}{r^2(1-M_r)^3}\right]_{\text{ret}} dS\right). \tag{7}$$

$f(x,t) = 0$ defines the surface of the solid body. r is the magnitude of the vector from the source point to the observer. M is the Mach number, defined as $M = v/c_0$, where v is the velocity of the surface and c_0 is the speed of sound. Mr is the Mach number in the radiation direction. A dot over a variable denotes differentiation with respect to time. The subscript "ret" denotes the retarded time. U_n and L_i are defined as shown in Eq. (8), where δ_{ij} is the Kronecker delta, u_n represents local normal velocity of the flow, and v_n represents local normal velocity of the surface. L_r is the component of L_i in the radiation direction and L_M represents a Mach-number-related correction term, which is obtained as the inner product of L_i with the local Mach number vector M_i,

$$\begin{cases} U_n = \left(1 - \frac{\rho}{\rho_\infty}\right)v_n + \frac{\rho u_n}{\rho_\infty}, \\ L_i = \left(p\delta_{ij}n_j + \rho u_i(u_n - v_n)\right). \end{cases} \tag{8}$$

D. Numerical setup

The coordinate system is set with the x axis pointing in the incoming flow direction and the z axis representing the spanwise direction. An O–H composite grid topology was employed in the computational domain spanning $-15 < x/D < 30$, $-15 < y/D < 15$, and $-\pi/2 < z/D < \pi/2$, as shown in Fig. 1. Within the range of $r = 7.5D$, an O-shaped grid with high orthogonality is adopted. D refers to the diameter of the cylinder, which is 0.000 86 m. The grid parameterization in the x–y planes followed the methodology established by Fan *et al.*,[27] with expansion ratios set at 1:6 for regions 1, 3, 5, and 7 as illustrated in Fig. 2. For the O-shaped grid, the circumferential mesh number is 240 and the radial mesh number is 200. The height of the first layer of mesh cells normal to the wall is $5.5 \times 10^{-3}D$. The maximum values of y^+, l^+, and s^+ are 3.28, 5.69, and 89.79, respectively, and the total number of the mesh is 1.28 million. Particular attention is given to maintaining natural grid transitions and ensuring uniform grid distribution along the z direction. Although the x–y plane mesh is designed based on the setup of Fan *et al.*[27] and is therefore considered reliable, the x–y mesh sensitivity analysis has been included in the Appendix for completeness.

In this study, the linear upwind stabilized transport (LUST) scheme is employed in the simulation. For the temporal discretization, a second-order implicit backward differencing scheme is adopted. The diffusion term is handled using a Gaussian linear conservative scheme. Pressure–velocity coupling is resolved through the PIMPLE algorithm.

III. RESULTS AND DISCUSSION

A. Study of spanwise grids and boundary conditions

According to the research,[36,37] the number of grids in the z direction and the boundary conditions have a significant impact on the simulation of the flow field. The settings of the spanwise grid and the statistics of the time-averaged flow field, including drag coefficient

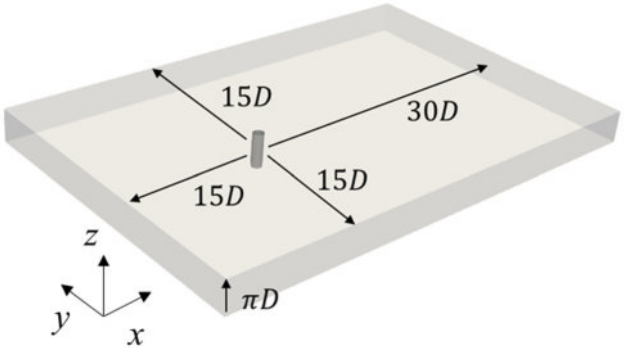

FIG. 1. Computational domain.

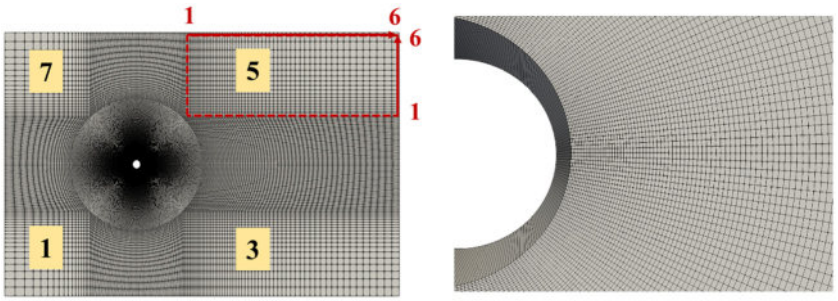

(a) Computational mesh in global view (b) Computational mesh in local view

FIG. 2. Mesh refinement in x–y plane.

(C_d), base pressure coefficient ($-C_{pbase}$), and Strouhal number (St), are shown in Table I. They are defined as

$$C_d = \frac{F_d}{\frac{1}{2}\rho_\infty U_\infty^2 A}, \tag{9}$$

$$C_p = \frac{p - p_0}{\frac{1}{2}\rho_\infty U_\infty^2}, \tag{10}$$

$$St = \frac{fD}{U_\infty}. \tag{11}$$

Here, F_d is the force acting on the cylinder in the x direction, ρ_∞ is the undisturbed far-field density of flow, U_∞ is the incoming flow velocity, A is the lateral projected area, p is the wall pressure, p_0 is the undisturbed far-field pressure, f is the frequency of the vortex shedding, and D is the diameter of the cylinder.

Given the critical role of the simulation of wake in acoustic field prediction, time-average profiles of the wake in different cases are shown in Figs. 3–6. All parameters are nondimensionalized using the flow velocity U_∞ or U_∞^2. The results were compared with the experimental values of Parnaudeau *et al.*[28] and the DNS results of Li *et al.*[38] For clarity of presentation, only representative flow field visualizations exhibiting substantial disparities are displayed, focusing on key differentiating features between cases.

Numerical investigations reveal superior flow field resolution at z-directional grid density $N_z = 22$, demonstrating optimal balance between computational accuracy and resource allocation. Parametric analysis indicates a monotonic relationship between spanwise grid refinement and aerodynamic coefficients: both drag coefficient (C_d) and base pressure coefficient ($-C_{pbase}$) exhibit decreasing trends with grid augmentation. This is mainly due to a slight overestimation of the length of the recirculation zone, which in turn leads to a relatively low drag coefficient, consistent with the earlier reports.[27,39–41]

Implementation of cyclic boundary conditions introduces measurable deviations for C_d and C_{pbase}, yet maintains physical validity within acceptable error thresholds compared with DNS.[38] Notably, the flow field data in the wake have been greatly improved, especially the Reynolds stress compared with Fan *et al.*[27] The refined stress field resolution enables more precise source localization,[42] critical for broadband noise prediction in wake-dominated flows.

Figure 7 compares the acoustic results of two cases with different spanwise boundary conditions, computed via the surface integral. A near-field upstream observer and a far-field observer are selected, with positions of 1.96D, 130°, in polar coordinates and −1.2D, 16.2D, in Cartesian coordinates, respectively. The ordinate is the nondimensionalized power spectral density, as shown in Eq. (12). In this context, F denotes the Fourier transform, $\overline{F}$ refers to the complex conjugate of F, fs indicates the frequency resolution, and $nfft$ represents the total number of data used in the Fourier transform. Pressure is nondimensionalized using the sound speed and density, while frequency is nondimensionalized using the sound speed and the diameter of the cylinder.

The results are benchmarked against the DNS results from Li *et al.*[38] and the surface-integral-based data from Zhou *et al.*[43] It can be found that after changing the boundary conditions to cyclic, the noise fits better in the high-frequency part. This enhancement correlates with improved Reynolds stress predictions, a critical mechanism for high-frequency noise generation dominated by turbulent stress fluctuations.

Following systematic evaluation of grid sensitivity and boundary impacts, the Case D configuration (featuring optimized mesh topology and cyclic boundary conditions) was selected for subsequent investigations. This decision prioritizes its demonstrated capability to resolve

TABLE I. Mesh setup and the time-averaged flow quantities.

Case	Grid number in z direction	Spanwise boundary condition	C_d	$-C_{pbase}$	St
A	30	Symmetry	0.987	0.845	0.206
B	22	Symmetry	1.002	0.889	0.206
C	21	Symmetry	1.06	0.912	0.198
D	22	Cyclic	1.1	0.97	0.209
Parnaudeau *et al.*[28](Exp)	···	···	0.99	0.88	0.208
Li *et al.*[38] (DNS)	···	···	1.04	0.94	0.205

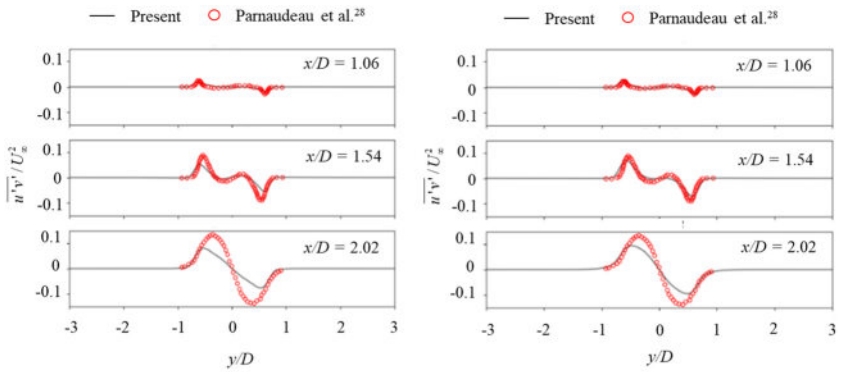

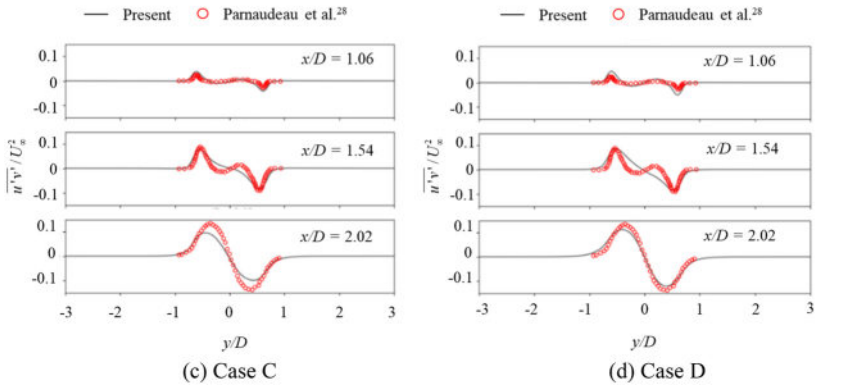

FIG. 3. Mean resolved Reynolds stress $\overline{u'v'}$ at $x/D = 1.06$, 1.54, and 2.02.

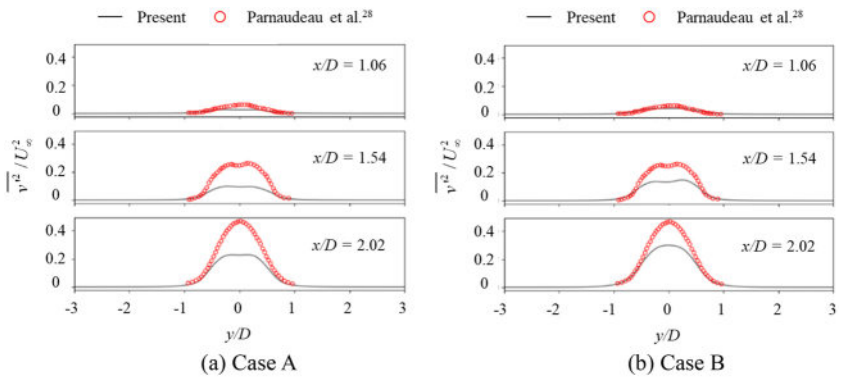

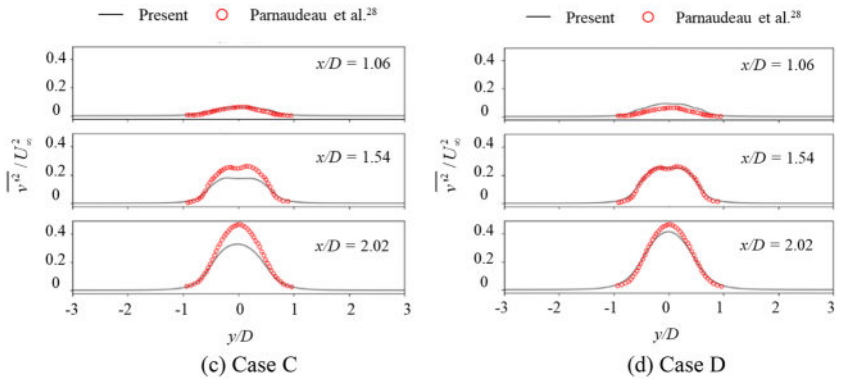

FIG. 4. Mean resolved Reynolds stress $\overline{v'v'}$ at $x/D = 1.06$, 1.54, and 2.02.

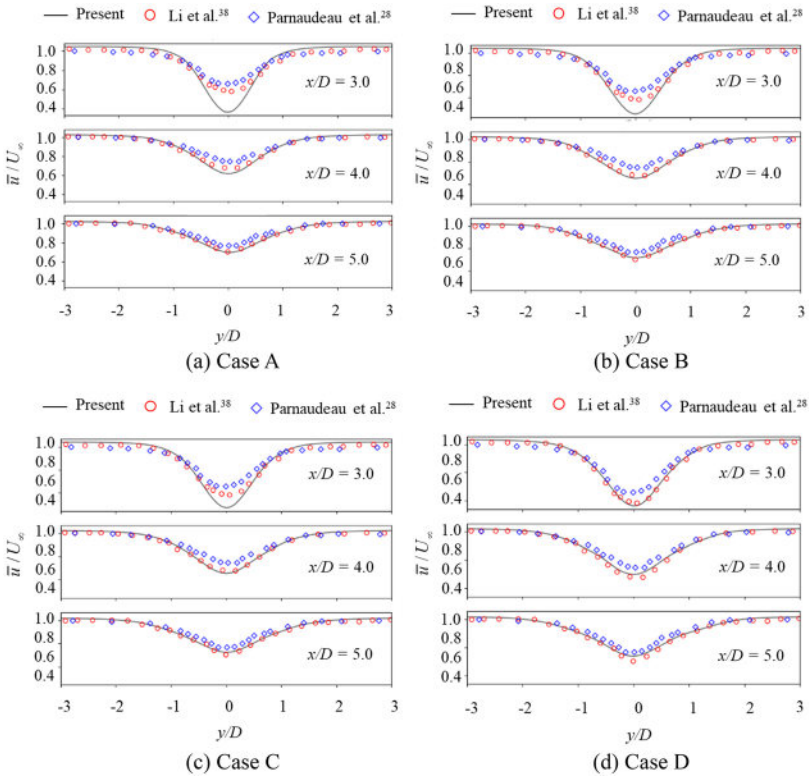

FIG. 5. Mean streamwise velocity profiles at $x/D = 3.0$, 4.0, and 5.0.

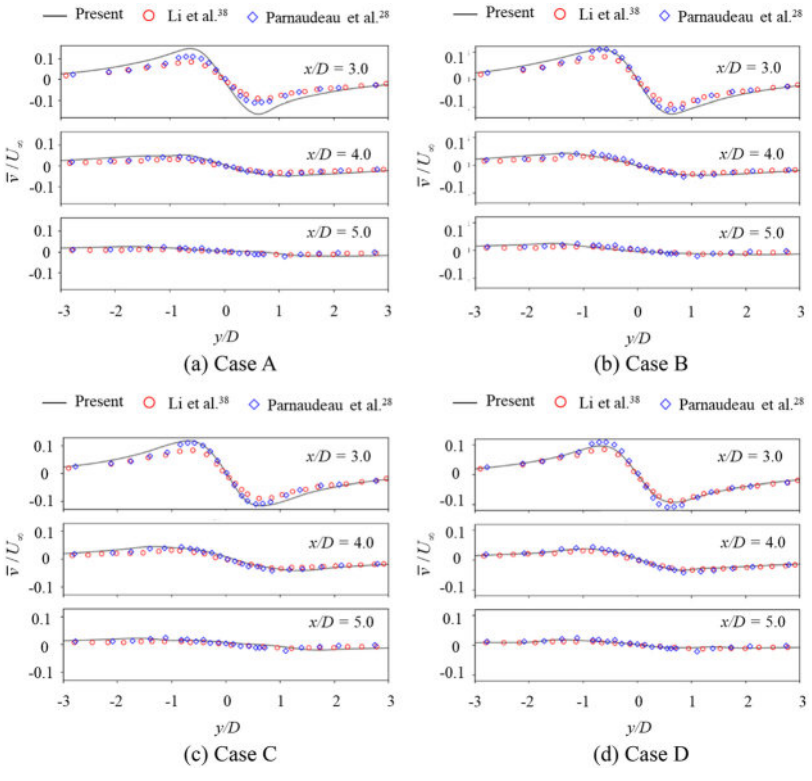

FIG. 6. Mean transverse velocity profiles at $x/D = 3.0$, 4.0, and 5.0.

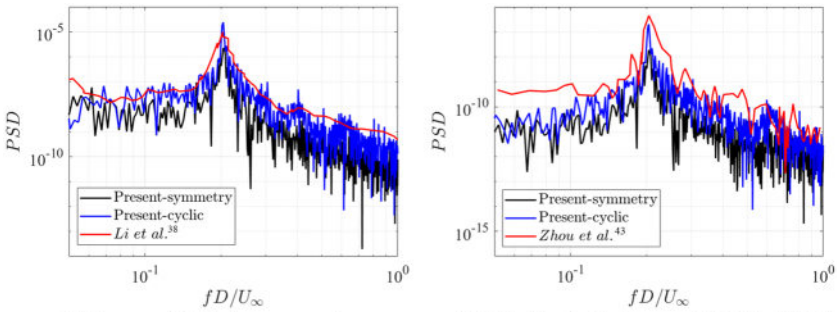

(a) The near-field observer upstream (1.96*D*, 130°)

(b) The far-field observer (-1.2*D*, 16.2*D*)

FIG. 7. The frequency spectrum of the acoustic data.

both aerodynamic and aeroacoustics phenomena with balanced computational fidelity, particularly critical for capturing broadband noise.

$$PSD = 2 \cdot F(p')\overline{F(p')}/(fs \cdot nfft). \tag{12}$$

B. Comparison of hydrodynamic and aerodynamic results

Numerical investigations of hydrodynamic circular-cylinder flows were conducted through changing the incoming flow velocity while maintaining constant *Re*. The grid and numerical schemes for the hydrodynamic case are the same as those of the aerodynamic one. The configurations of the two cases are shown in Table II. The incoming velocities are 68 and 4.535 m/s for the aerodynamic and hydrodynamic cases, respectively. In order to fully develop the flow field, 250 vortex shedding cycles were simulated.

The Mach number of the aerodynamic flow is 0.2, falling within the low-Mach-number regime. According to the research of Xue *et al.*,[44] for the flow with a Mach number less than 0.2, the influence of compressibility can be disregarded. As shown by Figs. 8 and 9, the results were compared with those from previous studies.[28,38,45] It demonstrates minimal divergence in normalized velocity profiles and pressure distributions between aerodynamic and hydrodynamic cases. The results are dimensionless by density and incoming flow velocity of air and water, respectively.

While the hydrodynamic and aerodynamic cases exhibit comparable flow field characteristics, their acoustic results show pronounced discrepancies due to orders-of-magnitude disparity in Mach numbers. Table III shows the root mean square (RMS) of sound pressure at three different observers, namely, the upstream observer in the near-field (1.96*D*, 130°), the downstream observer in the near-field (2.5*D*, 20°), and the far-field observer (−1.2*D*, 16.2*D*). The results are dimensionless by density and incoming flow velocity of air and water, respectively.

Comparative analysis reveals that for the near-field observers, the order of magnitude of the dimensionless values of the hydrodynamic noise and the aerodynamic noise is comparable, while in the far-field, the dimensionless RMS of the hydrodynamic noise is only 0.2 times that of the aerodynamic noise. To further investigate the far-field acoustic characteristics, 36 observers are uniformly distributed at

TABLE II. Computational configuration information of aero and hydro cases.

Case	Incoming velocity U_∞(m/s)	*Ma*	$\Delta t U_\infty/D$
Aerodynamic	68	0.2	0.0198
Hydrodynamic	4.535	0.0032	0.011

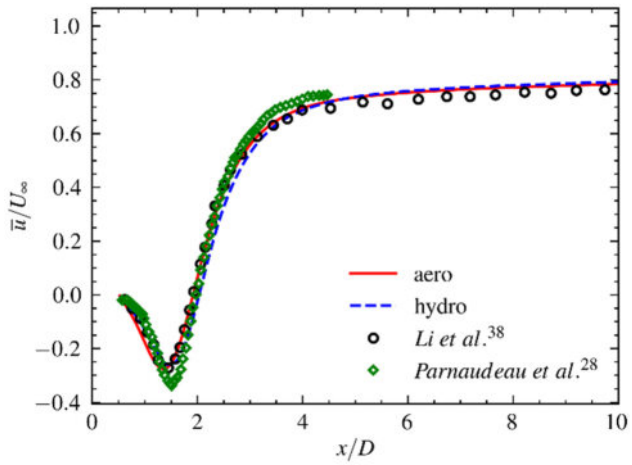

FIG. 8. Mean streamwise velocity profiles at $y/D = 0$.

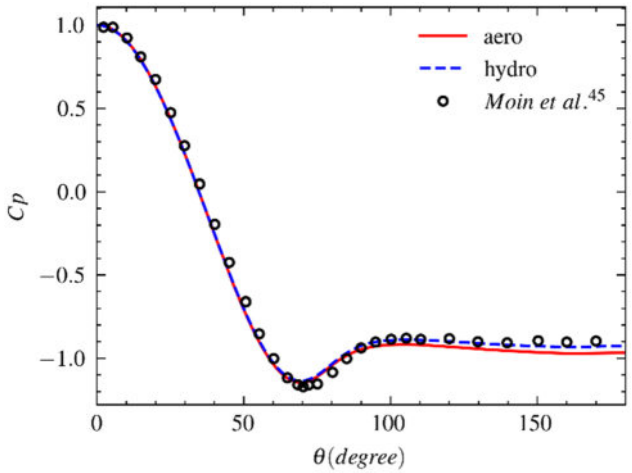

FIG. 9. Time-averaged pressure distribution on the cylinder surface.

TABLE III. The dimensionless value of the RMS of sound pressure.

Case	(1.96D, 130 °)	(2.5D, 20 °)	(−1.2D, 16.2D)
Aerodynamic	0.0121	0.0166	4.05×10^{-4}
Hydrodynamic	0.0114	0.0159	8.25×10^{-5}

$r = 23.06D$, and the corresponding acoustic directivity pattern is presented in Fig. 10. The radial axis represents the dimensionless RMS of the acoustic pressure. In the farther far field, the dimensionless acoustic pressure generated by hydrodynamic noise is significantly lower than that of aerodynamic noise, and its directivity is also much less pronounced. In the following, an analysis is conducted from the perspectives of sound sources and sound propagation to investigate the underlying reasons for the differences in near-field and far-field noise characteristics between aerodynamic and hydrodynamic cases.

C. Analysis of the source term

In this work, dynamic mode decomposition is employed, ranking mode energies at different frequencies from highest to lowest. The first three modes between the hydrodynamic and aerodynamic cases are compared as shown in Fig. 11. The first mode is the mean mode, corresponding to a frequency of zero. Dipole sound pressure exhibits a figure-eight distribution, with opposite signs on either side of the wall and maximum values occurring near the wall. This is directly related to the directional variation of the unsteady lift on the object's surface. The first-mode sound pressure levels of the hydrodynamic and aerodynamic cases are of comparable magnitude, with the hydrodynamic case being slightly higher. This indicates that, for sound radiation generated by steady-state components, the two cases have similar intensities, with the hydrodynamic case having a slight advantage. The key differences lie in the higher-order modes. In the hydrodynamic case, the sound pressure of higher-order modes decreases rapidly with increasing mode order, with magnitudes far lower than that of the first mode. In contrast, while the higher-order modes in the aerodynamic case also decay, their relative strengths are significantly higher than those in the hydrodynamic case. In other words, the hydrodynamic case is overwhelmingly dominated by the mean mode, with dipole sound radiation energy concentrated mainly in the low-frequency components and high-frequency contributions being negligible. In the aerodynamic case, although the mean mode still has the highest energy, the higher-order modes, particularly the first few, make non-negligible contributions. This is because the high-frequency wall pressure fluctuations are closely related to the interaction of small-scale shedding vortices with the wall surface as shown in Fig. 12. These small vortices rapidly dissipate kinetic energy through viscous effects, while the fluid in the hydrodynamic case has higher density and viscosity, making them inefficient at converting into radiated acoustic energy. As a result, dipole sources in hydrodynamic noise exhibit a strongly low-frequency and steady-state dominant characteristic.

Figure 13 presents contour maps of the root-mean-square wall pressure fluctuations for both cases. The maximum fluctuations occur at approximately 100° and 260°, which are closely associated with the regions of flow separation, enhanced shear-layer instability, and the onset of vortex shedding in the classic circular-cylinder wake. These regions also correspond to the directions of strongest sound pressure radiation identified in the Doppler-effect analysis. From 100° to 260°, corresponding to the upstream side of the cylinder, the pressure fluctuations are relatively weak and the flow remains laminar. Figure 14 shows the coherence spectra between the acoustic signals at seven observers located from 0° to 180°, and the strongest wall pressure signal at 100°. Coherence quantifies the degree of linear correlation between signals in the frequency domain. In both the hydrodynamic and aerodynamic cases, observer 0°, located farthest downstream, exhibits the lowest coherence, with peak values well below 0.5. This indicates that the wall pressure fluctuations at 100° have almost no direct influence at this location, which may partly explain the very low sound pressure levels at 0° in the directivity pattern. Although the coherence at 180° is relatively high, dipole radiation propagates primarily perpendicular to the incoming flow, so its sound pressure levels are also small. In the aerodynamic case, the coherence spectra exhibit clearer peak features, indicating a strong association between the sound field and wall pressure fluctuations at specific frequencies. In contrast, the

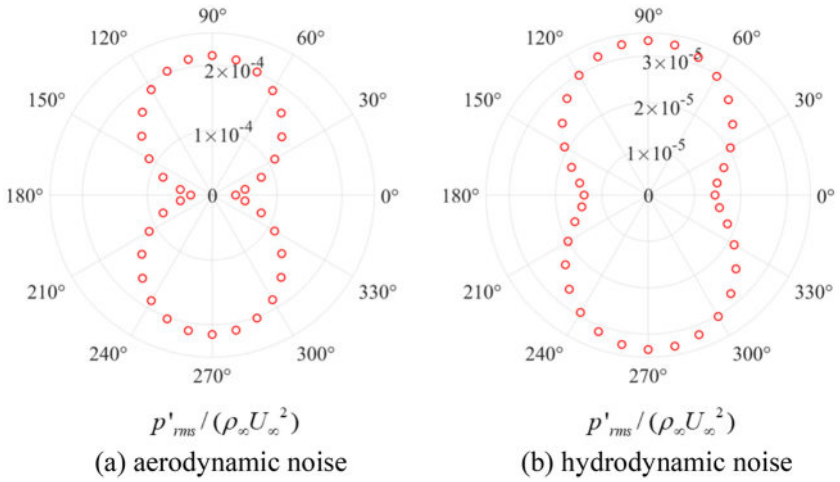

FIG. 10. Acoustic directivity diagram at $r = 23.06D$.

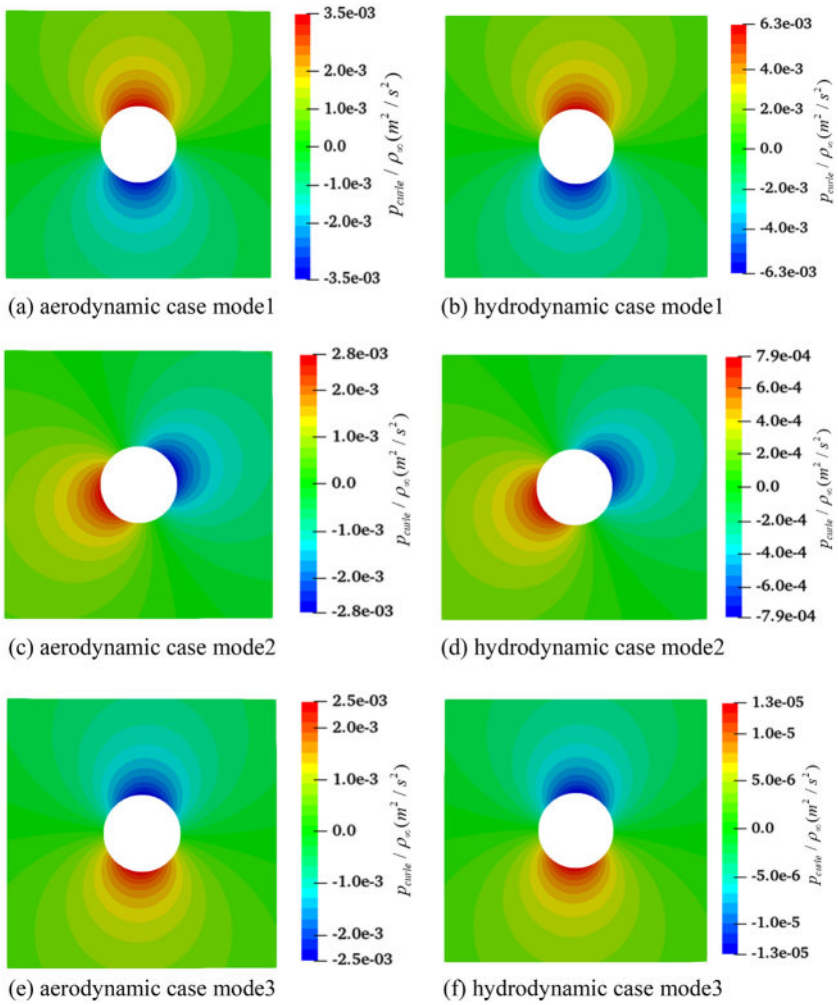

FIG. 11. Mode decomposition of dipole.

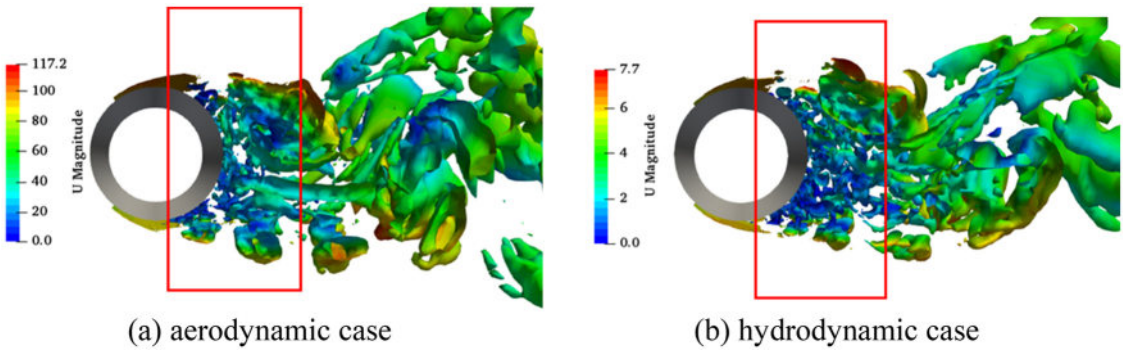

FIG. 12. Isosurface of vorticity with OmegaR = 0.62.

hydrodynamic case shows less distinct peak features in the coherence spectra, with the coherence at 0° nearly approaching zero. The coherence at 180° is also slightly lower than that at most other observers.

D. Analysis of sound propagation

To investigate the phenomenon of sound propagation with distance, observers are placed at a polar angle of $\theta = 130^\circ$, with radii of 1.96D, 23.06D, 40D, 60D, 80D, 100D, 120D, and 140D. Figure 15 is a

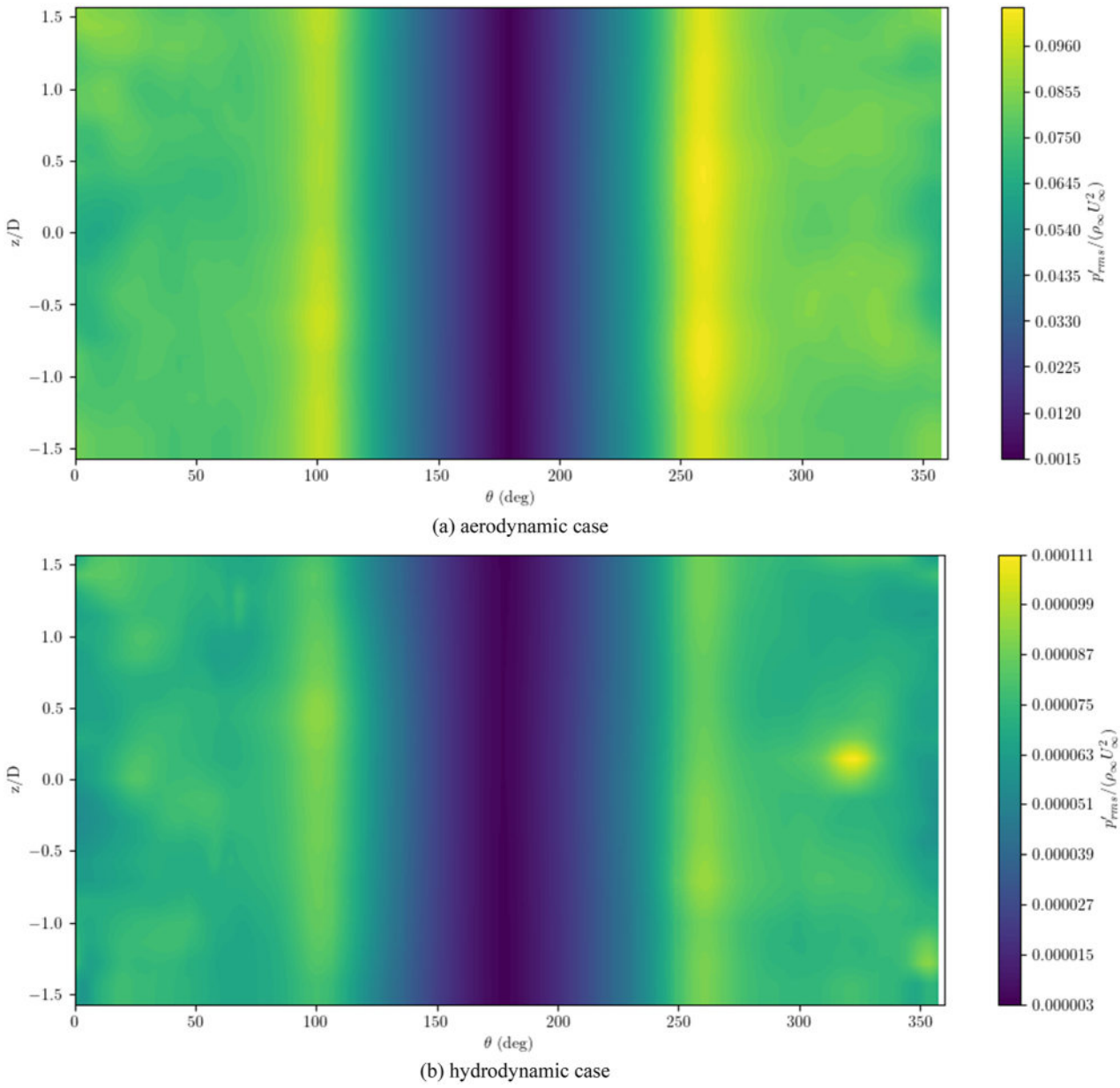

FIG. 13. RMS of the fluctuated wall pressure.

plot of sound pressure vs radial distance, revealing that hydrodynamic noise decays rapidly with increasing distance.

This divergence is very likely to stem from fundamental differences in propagating acoustic pressure contributions between the two regimes. According to the study by Li *et al.*,[38] regardless of whether the medium is water or air, the near-field fluctuating pressure can be decomposed into two parts: the acoustic component that can propagate to the far field and the hydrodynamic component, which decays rapidly and is also referred to as pseudo-sound. To isolate near-field hydrodynamic components from acoustic pressures easy to radiate, the wavelet decomposition technique is implemented. Figures 16 and 17 present the decomposition results.

The pseudo-sound component is illustrated by the blue curves in Figs. 16 and 17. The results of the wavelet decomposition are independent of the choice of far-field observation location.[38] In this study, the same far-field observer as that used by Li *et al.*[38] is adopted, with the polar radius equals to 23.06*D*.

Spectral analysis of the decomposed pressure fields reveals distinct radiation mechanisms between aerodynamic and hydrodynamic regimes. Although the pseudo-sound component dominates in both

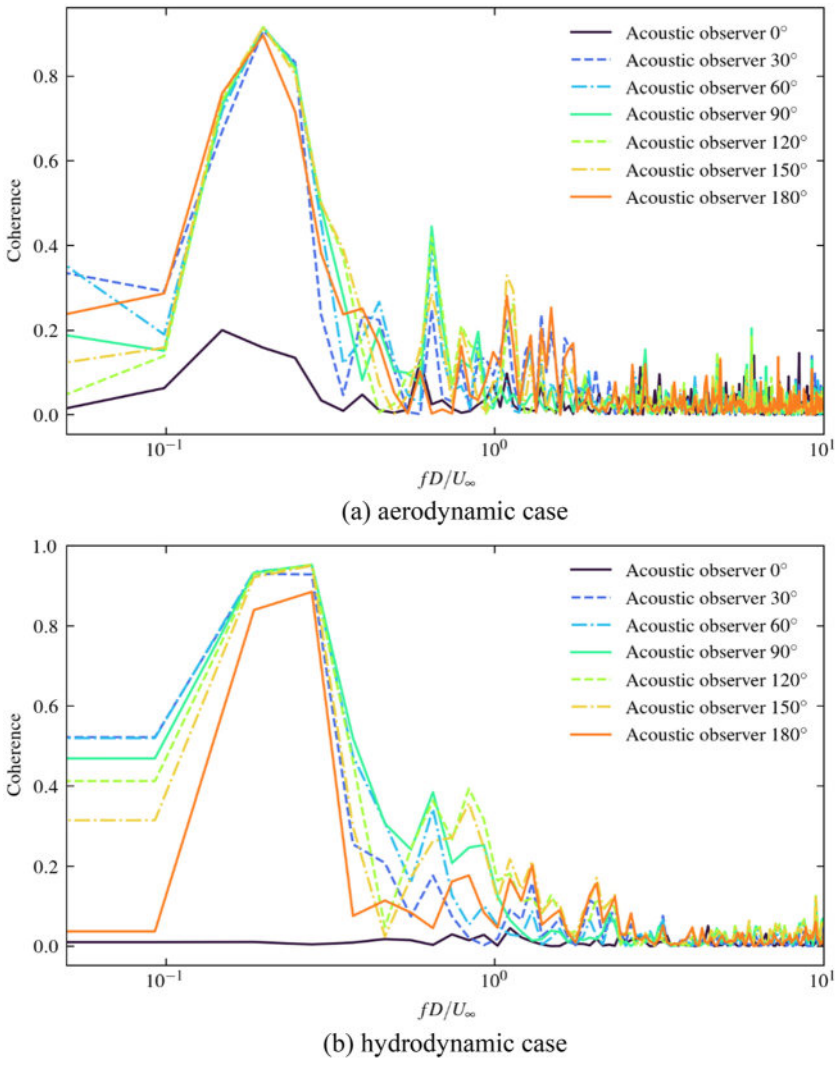

FIG. 14. Coherence between the acoustic signals and the wall pressure fluctuation signals at 100°.

aerodynamic and hydrodynamic cases, for aerodynamic noise, the upstream acoustic pressure is nearly comparable in magnitude to the pseudo-sound component, which means that the sound pressure at this location can be better transmitted to the far field. In contrast, the downstream region is primarily dominated by pseudo-sound, with only a negligible portion of acoustic pressure, suggesting viscous dissipation rapidly attenuates pressure perturbations within 2–3 characteristic lengths, effectively suppressing far-field radiation. For hydrodynamic noise, whether upstream or downstream, the proportion of acoustic components is relatively small. This leads to the fact that the far-field dimensionless RMS of sound pressure of hydrodynamic noise is much smaller than that of aerodynamic noise.

E. Conversion between hydrodynamic and aerodynamic noise outcomes

Turner and Kim[35] proposed the Mach number scaling for dipoles noise of different Mach numbers, where their ratio satisfies a power-law relationship with the Mach number. The scaling is employed in this paper to achieve the conversion between aerodynamic noise and hydrodynamic noise. There are two exponents for conversion, namely, *Na* and *Nu*, which each show certain advantages for observers at different angles. *Na* is a conversion exponent related to sound speed, which satisfies the following relationship:

$$\frac{W(St_a)|_{M_A}}{W(St_a)|_{M_B}} = \left(\frac{M_A}{M_B}\right)^{Na}, \tag{13}$$

where W represents the sound power spectrum based on the Strouhal number, as given by the following equation:

$$p_a(x,t) = p(x,t) - \overline{p}(x), \tag{14a}$$

$$p_a(x,f,T) = \int_{-T}^{T} p_a(x,t)e^{2\pi ift}dt, \tag{14b}$$

$$S_{ppa}(x,f) = \lim_{T\to\infty} \frac{P_a(x,f,T)P_a^*(x,f,T)}{T}, \tag{14c}$$

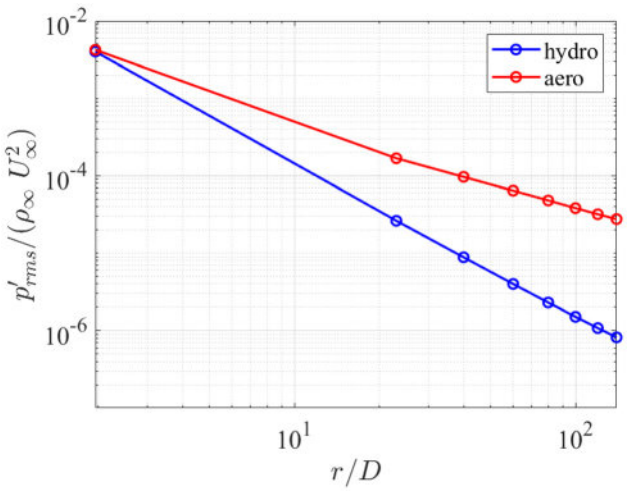

FIG. 15. RMS curve of sound pressure along radial positions.

where $*$ represents conjugate complex numbers

$$W(\theta_1,\theta_2,f)=\frac{Rb}{\rho_\infty a_\infty}\int_{\theta_1}^{\theta_2} S_{ppa}(\theta,f)d\theta. \tag{14d}$$

Among them, R is the distance from the center of the cylinder to the noise observers, taken as $23.06D$ in this part, and $b=\pi D$ is the spanwise length of the integral surface.

The other one is Nu, which is based on the incoming flow velocity and satisfies the following relationship:

$$\frac{W(St_u)|_{M_A}\times M_A}{W(St_u)|_{M_B}\times M_B}=\left(\frac{M_A}{M_B}\right)^{Nu}. \tag{15}$$

The Strouhal number is defined as follows, respectively:

$$\begin{cases} St_a = fD/a_\infty, \\ St_u = fD/U_\infty. \end{cases} \tag{16}$$

For comparison with Turner's results, the definition of θ_1,θ_2 here is consistent with that in Turner's paper, 10° less than θ_0 and 10° more than θ_0, respectively, where θ_0 is the middle observer angle, including 60°, 90°, 120°, and 150°. The results of Na for these angles are shown in Fig. 18.

Owing to the structural symmetry of the cylinder, the values of Na exhibit minimal variations across all observer angles. At every angle, a conspicuous peak occurs around $St_a=0.04$, indicating the maximum ratio of aerodynamic to hydrodynamic noise at this dimensionless frequency. As frequency increases, Na converges to a stable mean value of approximately 5, aligning closely with Turner's reported Na for airfoil dipoles.

In contrast to Na, Nu demonstrates small variations across frequencies. Turner's study noted significant angular variations in Nu for airfoils: $Nu=6$ near the leading edge vs $Nu=2$ at the trailing edge. For cylinders, however, Nu shows limited angular dependence with a mean value around 4 as shown in Fig. 19.

It is observed that Nu exhibits minimal variation across different angles, enabling its use for aerodynamic–hydrodynamic noise conversion

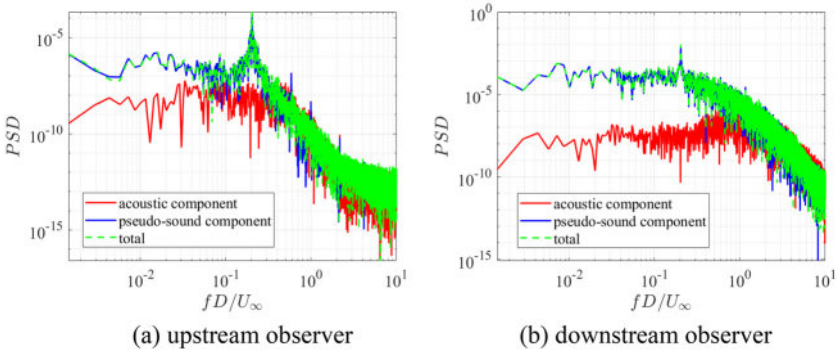

FIG. 16. Wavelet decomposition of aerodynamic sound pressure.

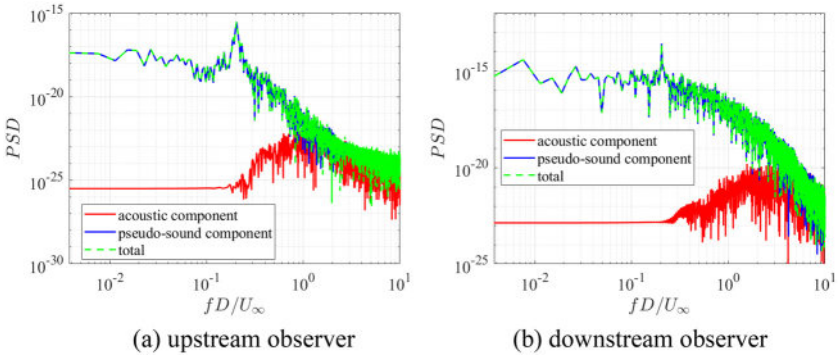

FIG. 17. Wavelet decomposition of hydrodynamic sound pressure.

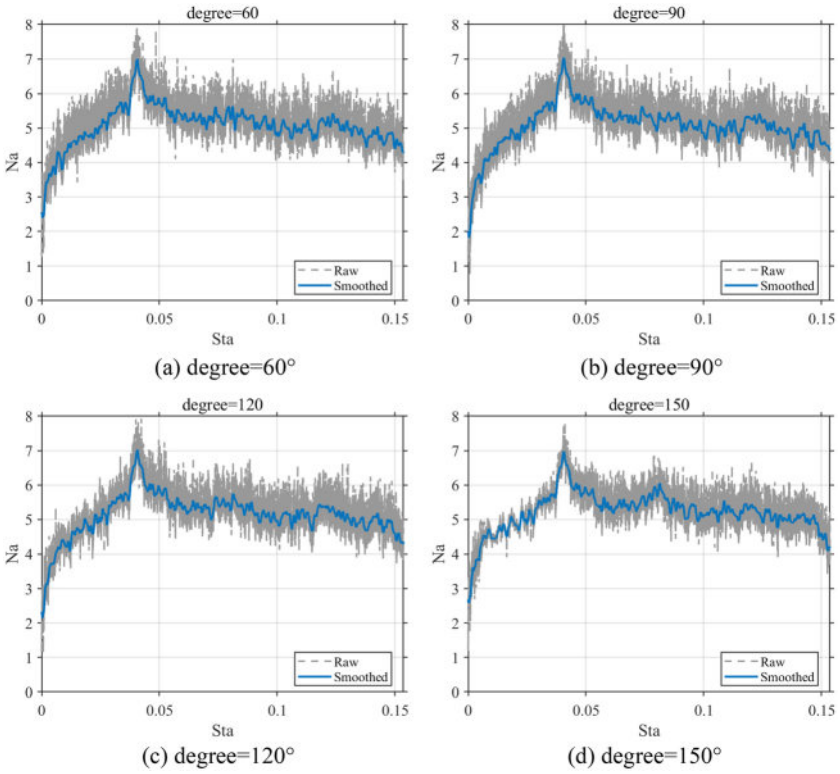

FIG. 18. Mach number scaling exponent *Na* between aerodynamic and hydrodynamic noise.

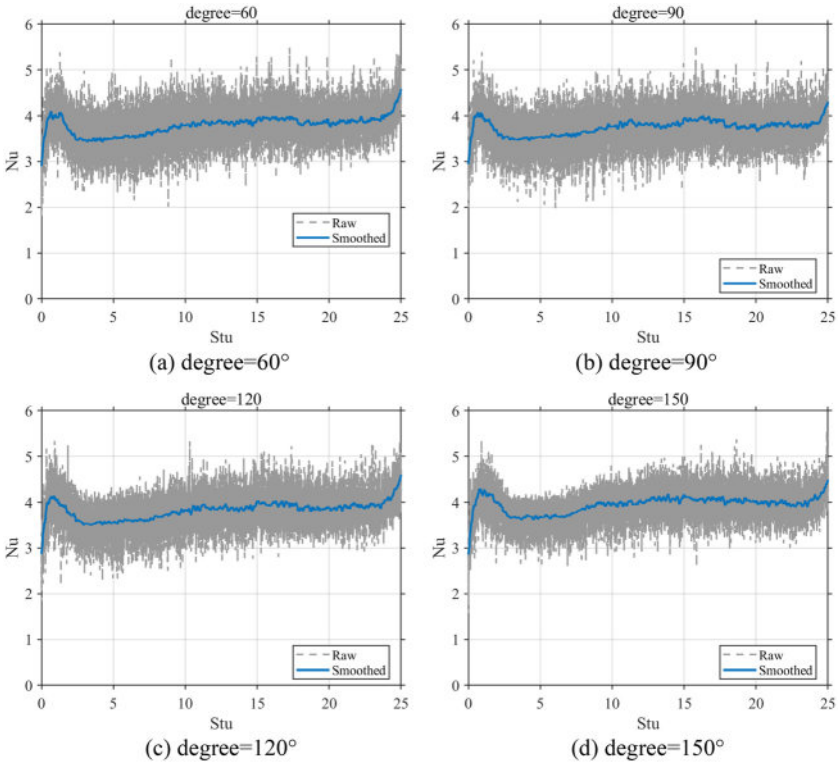

FIG. 19. Mach number scaling exponent *Nu* between aerodynamic and hydrodynamic noise.

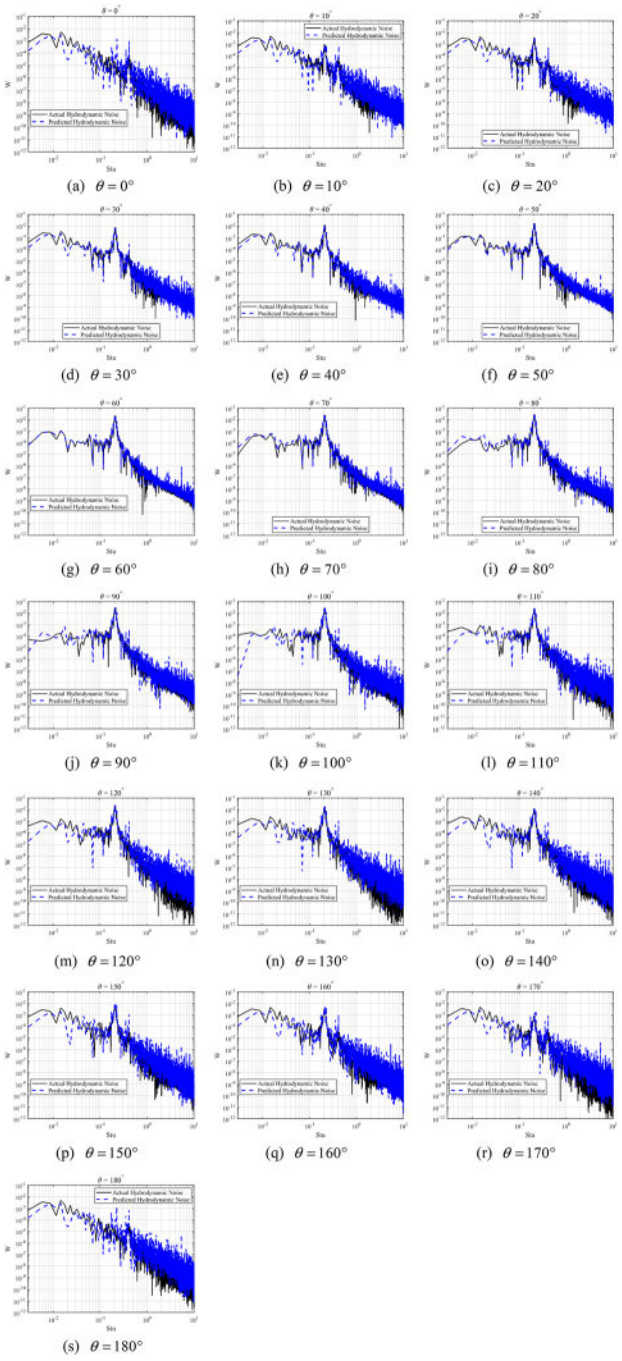

FIG. 20. Comparison of the predicted hydrodynamic noise and the actual results at observers with the same radius but different angles using *Nu*.

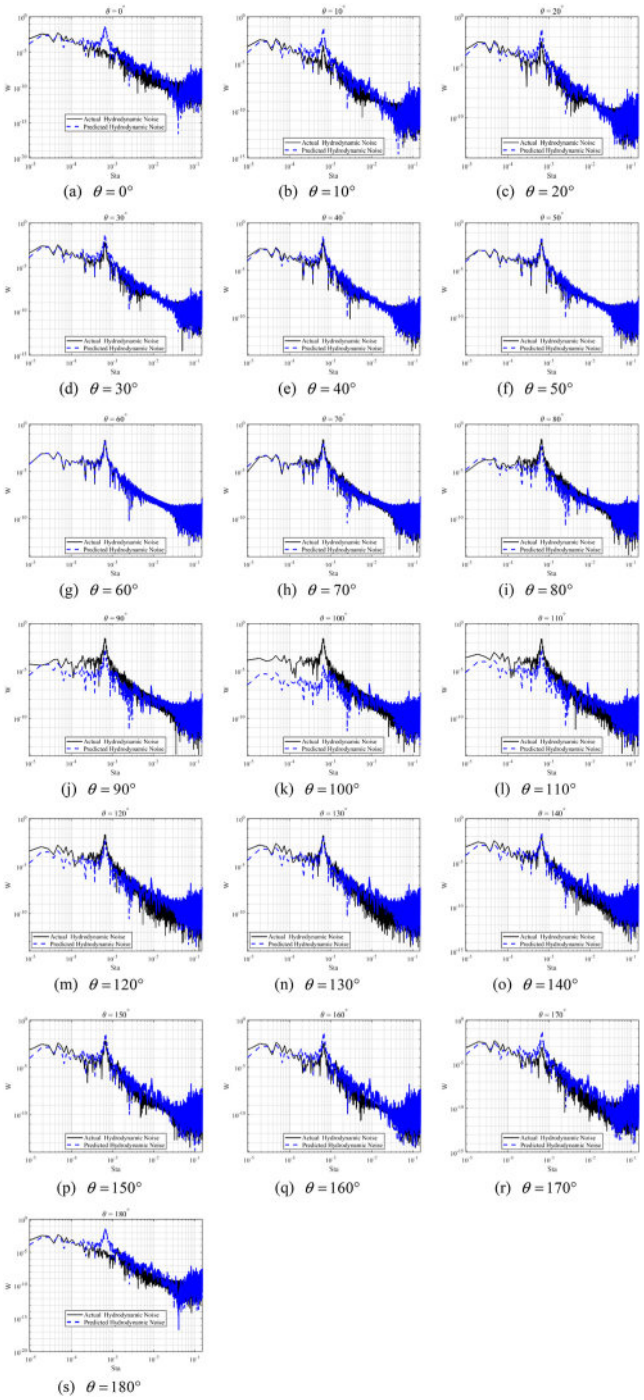

FIG. 21. Comparison of the predicted hydrodynamic noise and the actual results at observers with the same radius but different angles using *Na*.

regardless of angular position. $\theta_2 = \theta_1 = \theta_0$ is defined hereafter. Here, we first arbitrarily select an angle of 60° as the reference. Using the calculated *Nu* of $R = 23.06D$ and $\theta = 60°$, aerodynamic noise is converted to hydrodynamic noise via Eq. (15) and compared against actual hydrodynamic noise at the other 17 angles. Figure 20 demonstrates effective cross-angle conversion using *Nu*, with slight discrepancies at low frequencies but excellent agreement at spectral peaks, which is the most critical. This implies that *Nu* remains

effectively constant for fixed radius between different angles. Knowledge of *Nu* at a single point thus suffices to determine aerodynamic–hydrodynamic noise relationships at other locations with constant radius, enabling rapid prediction of hydrodynamic noise from aerodynamic data. Moreover, it can be observed that for a given radius, the *Nu* values at different angular positions exhibit only minor variations. Consequently, any angular position may serve as a valid reference for conversion. While the present study adopts the 60° position as the reference, alternative angles are equally applicable.

However, this conversion requires extrapolation because the hydrodynamic Strouhal number based on the velocity of incoming flow exceeds the aerodynamic value. This induces high-frequency distortion necessitating data filtering, which truncates the usable frequency range. Consequently, the predicted hydrodynamic noise spectrum typically displays a reduced bandwidth compared to empirical results.

Based on the discussion of Fig. 18, *Na* seems to work too. However, the apparent uniformity of *Na* across angles is actually attributable to angular selection bias. In reality, *Na* values diverge significantly across most angular positions, particularly at peak frequencies. Results are presented in Fig. 21. The conversion within the ranges of 30°–80° and 120°–160° shows good agreement if the *Na* in 60° is taken as the reference, whereas deviations at other angular positions are considerably larger. This contrasts with *Nu*, where the value at any angle can be adopted as a reference. Therefore, *Na* is unsuitable for noise conversion across different angular positions at the same radius due to its angular dependence.

For observers at identical angular positions but varying radial distances, *Na* effectively achieves conversion between aerodynamic and hydrodynamic noise. As observers at different radii are available solely at $\theta = 130°$ in the present study, the *Na* at 130° is adopted as the reference for the conversions in this part. Based on the *Na* value derived at $\theta = 130°$ and $R = 23.06D$, conversions were performed for other radial positions $R = 40D$, $60D$, $80D$, $100D$, $120D$, and $140D$. The predicted hydrodynamic noise results demonstrate robust consistency when compared against empirical data, as validated in Fig. 22. Crucially, unlike the frequency-scaling challenge noted earlier, no extrapolation is required here since the hydrodynamic Strouhal number based on the sound speed is smaller than its aerodynamic counterpart in numerical value. It is also observed that, for the same angular position, the *Na* values at different radii are nearly identical. In this part, $R = 23.06D$ is used as the reference, but other radii are equally applicable.

Consequently, we establish the law that for observers sharing identical radius but differing angular positions, *Nu* achieves effective conversion between aerodynamic and hydrodynamic noise. For observers sharing identical angle but varying radial distances, *Na* proves effective in this case.

By combining *Na* and *Nu*, full-field hydrodynamic noise predictions can be derived using either parameter from a single point

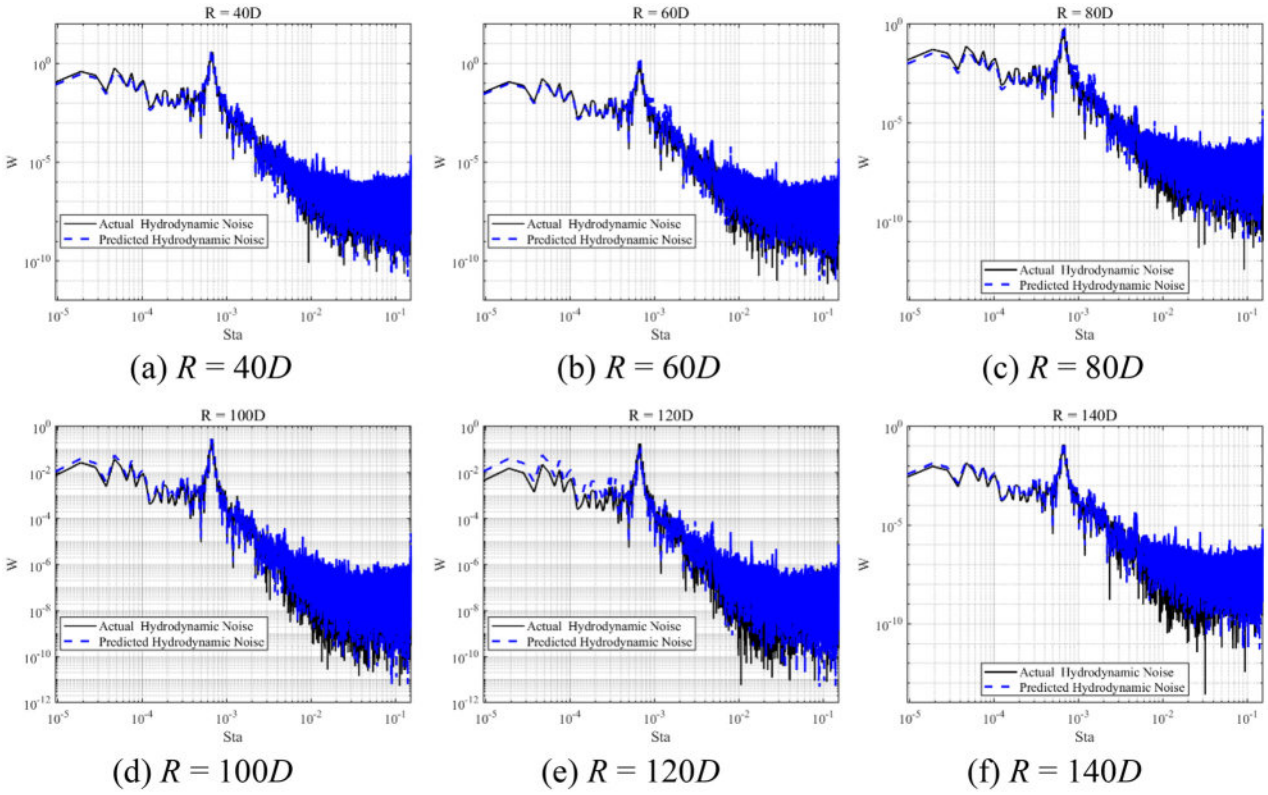

FIG. 22. Comparison of the predicted hydrodynamic noise and the actual results at observers with the same angle but different radii using *Na*.

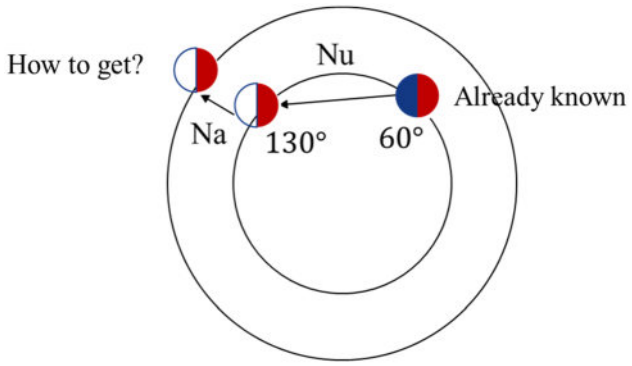

FIG. 23. Schematic diagram of noise conversion between aerodynamic and hydrodynamic noise at different positions.

alongside local aerodynamic data. This methodology is schematically illustrated in Fig. 23, where red semicircles denote locations with known aerodynamic noise and blue semicircles represent points possessing hydrodynamic noise data. Here, only the conversion from $R = 23.06D$, $\theta = 60°$ to $R = 140D$, $\theta = 130°$ is presented. Observers at other radii and angles can likewise be converted using this method.

For instance, to predict hydrodynamic noise at $R = 140D$, $\theta = 130°$ using data from $R = 23.06D$, $\theta = 60°$, the procedure is as follows. First, through the known hydrodynamic and aerodynamic noise data at $R = 23.06D$, $\theta = 60°$, we could get conversion exponent *Nu* of the positions with the same radius. Second, measure the aerodynamic noise at $\theta = 130°$, $R = 23.06D$ and $\theta = 130°$, $R = 140D$ (readily obtainable). Then, convert the hydrodynamic noise at $\theta = 130°$, $R = 23.06D$ by the aerodynamic noise using *Nu*. Subsequently, derive *Na* at this angular position using the converted hydrodynamic data and measured aerodynamic noise. Finally, apply this *Na* value to the aerodynamic noise at $\theta = 130°$, $R = 140D$ to obtain the predicted hydrodynamic noise. Figure 24 compares the predicted and actual hydrodynamic results, demonstrating excellent agreement.

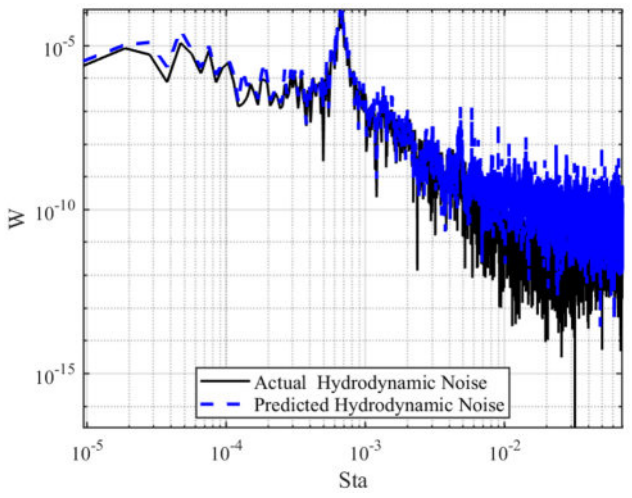

FIG. 24. Comparison of the predicted hydrodynamic noise and the actual results at observers with different angles and radii using *Na* and *Nu*.

This approach is expected to be highly effective for experimental applications. Since aerodynamic noise data from wind tunnel tests are readily obtainable, while hydrodynamic measurements often suffer from inaccuracies due to low SNR, the conversion framework offers significant practical value. Provided aerodynamic noise measurements are available across the field (typically accessible in experiments), selecting a strategically locate point with sufficient hydrodynamic SNR allows accurate determination of either *Na* or *Nu*. This calibrated parameter then enables prediction of hydrodynamic noise at any arbitrary position using local aerodynamic data, constituting the core practical significance of this conversion methodology. Notably, while this paper focuses on $Re = 3900$, the proposed noise conversion framework is not restricted to this Reynolds number. The formulation of *Na* and *Nu* is dimensionless and based on Mach-number scaling, which remains physically valid at higher Reynolds numbers as long as the dominant source mechanism remains dipolar. We are currently extending this framework to higher Reynolds numbers for SUBOFF. These results will be included in a follow-up study.

IV. CONCLUSIONS

In this paper, the flow past a cylinder at $Re = 3900$ is used as the research object based on the OpenFOAM to explore the differences between aerodynamic and hydrodynamic noise and their conversion relationship. The flow field is simulated using a wall-modeled large eddy simulation (WMLES) based on the non-equilibrium ODE-based wall model (NEWQM), while the acoustic field is computed through surface integration of the Ffowcs Williams–Hawkings (FW-H) equation. The article employs methods including dynamic mode decomposition (DMD), coherence analysis, and wavelet decomposition to analyze flow field statistics, sound sources, sound propagation, and noise results. The main conclusions are as follows.

Aerodynamic and hydrodynamic noise with the same Reynolds number exhibit fundamentally different far-field behaviors despite similar near-field magnitudes and the noise disparity primarily stems from sound source characteristics and sound propagation mechanisms. The analysis reveals that while the first-mode dipole sound pressure are comparable between the hydrodynamic and aerodynamic cases, the spectral distribution differs fundamentally. Hydrodynamic noise is strongly dominated by the mean mode, with negligible contributions from higher-order modes. In contrast, aerodynamic noise exhibits appreciable contributions from the first few higher-order modes and it exhibits distinct coherence peaks at specific frequencies, highlighting a strong coupling between the wall pressure and the radiated sound field.

Pseudo-sound dominates both flow types, but its contribution to the total pressure differs markedly between aerodynamic and hydrodynamic cases. For aerodynamic noise, the upstream acoustic pressure is nearly comparable in magnitude to the pseudo-sound component, which means that the sound pressure at this location can be better transmitted to the far field. In contrast, the downstream region is primarily dominated by pseudo-sound, with only a negligible portion of acoustic pressure. For hydrodynamic noise, whether upstream or downstream, the proportion of acoustic components is relatively small. This leads to the fact that the dimensionless far-field RMS of sound pressure of hydrodynamic noise is much smaller than that of aerodynamic noise though the magnitude of the near-field sound pressure is comparable.

The most important finding is that the proposed Mach-number-based conversion exponents *Na* and *Nu* enable quantitative and directional mapping between aerodynamic and hydrodynamic noise spectra. The analysis shows that *Nu* exhibits minimal angular dependence, enabling effective cross-angle conversions. It can be determined from hydrodynamic and aerodynamic data at a single angular location and then applied robustly to predict hydrodynamic noise at other angular positions with the same radius without significant loss of accuracy. In contrast, *Na* displays pronounced angular variability, limiting its applicability across different angles. However, *Na* remains consistent across varying radii at fixed angles, where it achieves highly accurate conversions without the frequency-scaling challenges encountered in angular cases. By synergistically applying these two exponents, a quantitative mapping relationship between the full-field aerodynamic and hydrodynamic noise spectrum can be established.

ACKNOWLEDGMENTS

This work was supported by the National Natural Science Foundation of China (52201372 and 52131102), to which the authors are most grateful.

AUTHOR DECLARATIONS

Conflict of Interest

The authors have no conflicts to disclose.

Author Contributions

Jiajia Qin: Data curation (equal); Formal analysis (equal); Investigation (equal); Methodology (equal); Software (equal); Writing – original draft (equal). **Haiting Yu:** Conceptualization (equal); Methodology (equal); Validation (equal). **Decheng Wan:** Funding acquisition (equal); Project administration (equal); Resources (equal); Supervision (equal); Writing – review & editing (equal). **Yuan Zhuang:** Funding acquisition (equal); Visualization (equal); Writing – review & editing (equal).

DATA AVAILABILITY

The data that support the findings of this study are available from the corresponding author upon reasonable request.

APPENDIX: MESH SENSITIVITY ANALYSIS FOR THE X-Y PLANE

Here, the mesh sensitivity analysis for the *x-y* plane is presented. Three mesh resolutions (fine, medium, and coarse) were designed, with the grid spacing in the *x* and *y* directions increasing by a factor of $\sqrt{2}$ between cases, while the number of grids in the *z* direction was kept constant at 22. The mesh information and corresponding flow field results are shown below. It can be observed that the flow field of case B shows significant improvement compared with case C, whereas further refinement results in only minor changes. Therefore, considering both computational efficiency and accuracy, case B is deemed appropriate for the present study (Tables IV and V).

TABLE IV. Mesh refinement for *x–y* plane.

Case	$\Delta y/D$	$\Delta x/D$	N_{total} (million)
A	3.9×10^{-3}	9.3×10^{-3}	2.57
B	5.5×10^{-3}	1.3×10^{-2}	1.28
C	7.7×10^{-3}	1.9×10^{-2}	0.63

TABLE V. Mesh quality effect on the mean flow parameters.

Case	C_d	$-C_{pbase}$	St
A	1.09	0.99	0.206
B	1.1	0.97	0.209
C	1.21	1.06	0.197
Parnaudeau *et al.*[28](Exp)	0.99	0.88	0.208
Li *et al.*[38] (DNS)	1.04	0.94	0.205

REFERENCES

[1]W. Mao, H. Iacovides, A. Cioncolini, H. Li, and M. R. A. Nabawy, "A validated numerical methodology for flow-induced vibration of a semi-spherical end cantilever rod in axial flow," Phys. Fluids **36**(7), 515063 (2024).
[2]Y. Wei, Y. Wang, K. Ding, and J. Fu, "Submarine underwater structure-borne noise and flow noise due to propeller excitation," Acoust. Aust **40**(2), 122–127 (2012).
[3]Y. Song, P. Ming, and B. Xun, "Research on similarity law of the flow-induced noise of the submarine," J. Acoust. Soc. Am. **156**(6), 4010–4023 (2024).
[4]J. Zou, Y. Lv, H. Lan, and J. Shi, "Experimental research on an ocean vector noise field," J. Harbin Eng. Univ. **32**(1), 16–20 (2011).
[5]P. A. Lepper and S. P. Robinson, "Measurement of underwater operational noise emitted by wave and tidal stream energy devices," in *The Effects of Noise on Aquatic Life II* (Springer-New York, 2016), pp. 615–622.
[6]T. Ahlefeldt and C. Spehr, "Development of the microphone-array measurement technique for use in cryogenic and pressurized wind turbines," in 43rd International Congress on Noise Control Engineering, 2014.
[7]J. Webster, R. Raspet, J. Yu, and W. E. Prather, "Measurement of wind noise levels in streamlined observers," J. Acoust. Soc. Am. **127**(5), 2764–2770 (2010).
[8]G. W. Gu and B. Z. Zhu, "Measurement and spectrum analysis of background noise of aeroacoustic wind tunnel," Noise Vib. Control **31**(2), 156 (2011).
[9]G. M. Lilley, "The source of aerodynamic noise," Int. J. Aeroacoust. **2**(3), 241–253 (2003).
[10]H. V. Fuchs and A. Michalke, "Introduction to aerodynamic noise theory," Prog. Aerosp. Sci. **14**, 227–297 (1973).
[11]L. A. Bazhenova, "Noise sources of aerodynamic origin in air blowers," Acoust. Phys. **64**(3), 356–364 (2018).
[12]M. Terracol, E. Manoha, C. Herrero, E. Labourasse, S. Redonnet, and P. Sagaut, "Hybrid methods for airframe noise numerical prediction," Theor. Comput. Fluid Dyn. **19**, 197–227 (2005).
[13]C. Talotte, "Aerodynamic noise: A critical survey," J. Sound Vib. **231**(3), 549–562 (2000).
[14]W. De Roeck, W. Desmet, M. Baelmans, and P. Sas, "An overview of high-order finite difference schemes for computational aeroacoustics," in *Proceedings of the International Conference on Noise and Vibration Engineering* (KU Leuven, 2004), pp. 353–368.
[15]J. D. Revell, R. A. Prydz, and A. P. Hays, "Experimental study of aerodynamic noise vs drag relationships for circular cylinders," AIAA J. **16**(9), 889–897 (1978).
[16]D. J. Thompson, E. L. Iglesias, X. Liu, J. Zhu, and Z. Hu, "Recent developments in the prediction and control of aerodynamic noise from high-speed trains," Int. J. Rail Transp. **3**(3), 119–150 (2015).
[17]J. E. F. Williams and D. L. Hawkings, "Sound generation by turbulence and surfaces in arbitrary motion," Philos. Trans. R. Soc. A **321**, 321–342 (1969).

[18]Z. Nitzkorski and K. Mahesh, "A dynamic end cap technique for sound computation using the Ffowcs Williams and Hawkings equations," Phys. Fluids **26**(11), 115101 (2014).
[19]Z. Zheng, "Prediction of dipole sources and aeroacoustics field for tandem cylinder flow field based on DBEM/hybrid LES," Int. J. Aeroacoust. **20**(1-2), 157–173 (2021).
[20]O. Inoue and N. Hatakeyama, "Sound generation by a two-dimensional circular cylinder in a uniform flow," J. Fluid Mech. **471**, 285–314 (2002).
[21]R. D. Sandberg, N. D. Sandham, and P. F. Joseph, "Direct numerical simulations of trailing-edge noise generated by boundary-layer instabilities," J. Sound Vib. **304**(3–5), 677–690 (2007).
[22]R. D. Sandberg and N. D. Sandham, "Direct numerical simulation of turbulent flow past a trailing edge and the associated noise generation," J. Fluid Mech. **596**, 353–385 (2008).
[23]J. Kim and H. J. Sung, "Wall pressure fluctuations and flow-induced noise in a turbulent boundary layer over a bump," J. Fluid Mech. **558**, 79–102 (2006).
[24]N. Curle, "The influence of solid boundaries upon aerodynamic sound," Proc. R. Soc. A **231**, 505–514 (1955).
[25]A. Powell, "Aerodynamic noise and the plane boundary," J. Acoust. Soc. Am. **32**(8), 982–990 (1960).
[26]A. Posa and E. Balaras, "A numerical investigation about the effects of Reynolds number on the flow around an appended axisymmetric body of revolution," J. Fluid Mech. **884**, A41 (2020).
[27]G. Fan, Y. Liu, W. Zhao, and D. Wan, "Effect of wall stress models and subgrid-scale models for flow past a cylinder at Reynolds number 3900," Phys. Fluids **36**(1), 015152 (2024).
[28]P. Parnaudeau, J. Carlier, D. Heitz, and E. Lamballais, "Experimental and numerical studies of the flow over a circular cylinder at Reynolds number 3900," Phys. Fluids **20**(8), 085101 (2008).
[29]M. Liu, S. Zhang, Y. Li, and J. Qin, "Numerical investigation of flow over a finite length inclination circular cylinder under Re = 3900," Ocean Eng. **300**, 117262 (2024).
[30]J. Franke and W. Frank, "Large eddy simulation of the flow past a circular cylinder at $Re_D = 3900$," J. Wind Eng. Ind. Aerodyn. **90**(10), 1191–1206 (2002).
[31]J. Jacob and S. K. Bhattacharyya, "Numerical study on aerodynamic and hydrodynamic noise from circular cylinders," in *Proceedings of the Global Oceans 2020: Singapore – U.S. Gulf Coast* (IEEE, 2020).
[32]C. Poggi, G. Bernardini, M. Gennaretti, and R. Camussi, "Scalability of Mach number effects on noise emitted by side-by-side propellers," Appl. Sci. **12**(19), 9507 (2022).
[33]F. Farassat, "Derivation of formulations 1 and 1A of Farassat," Technical Report No. NASA/TM-2007-214853 (NASA, 2007).
[34]S. Jiang, Y. Wang, Z. Yan, R. Zhang, and Z. Hu, "Variations with Mach number for gust–airfoil interaction noise," Phys. Fluids **35**(2), 026111 (2023).
[35]J. M. Turner and J. W. Kim, "Quadrupole noise generated from a low-speed aerofoil in near- and full-stall conditions," J. Fluid Mech. **936**, A34 (2022).
[36]S. Rezaeiravesh and M. Liefvendahl, "Effect of grid resolution on large eddy simulation of wall-bounded turbulence," Phys. Fluids **30**(5), 055106 (2018).
[37]X. Liu and Y. Jiang, "Direct numerical simulations of boundary condition effects on the propagation of density current in wall-bounded and open channels," Environ. Fluid Mech. **14**(2), 387–407 (2014).
[38]S. Li, D. E. Rival, and X. Wu, "Sound source and pseudo-sound in the near field of a circular cylinder in subsonic conditions," J. Fluid Mech. **919**, A43 (2021).
[39]H. Jiang and L. Cheng, "Large-eddy simulation of flow past a circular cylinder for Reynolds numbers 400 to 3900," Phys. Fluids **33**(3), 034119 (2021).
[40]H. Ali, N. B. Khan, M. Jameel, A. Khan, M. Sajid, A. Munir, A. E. Ahmed, K. A. M. Alharbi, and A. M. Galal, "Numerical investigation of the effect of spanwise length and mesh density on flow around cylinder at Re = 3900 using LES model," PLoS One **17**(4), e0266065 (2022).
[41]N. B. Khan, Z. Ibrahim, A. B. B. M. Badry, M. Jameel, and M. F. Javed, "Numerical investigation of flow around cylinder at Reynolds number = 3900 with large eddy simulation technique: Effect of spanwise length and mesh resolution," Proc. Inst. Mech. Eng., Part M **233**(2), 417–427 (2019).
[42]J. C. Hardin, "Acoustic sources in the low Mach number turbulent boundary layer," J. Acoust. Soc. Am. **90**(2), 1020–1031 (1991).
[43]Z. Zhou, Y. Liu, and S. Wang, "Frequency-domain quadrupole correction for the permeable-surface Ffowcs Williams and Hawkings integration," Phys. Fluids **36**(7), 077137 (2024).
[44]K. Xue, Q. Li, and L. Zhao, "Compressibility effect on flow characteristics over a circular cylinder at Reynolds number of 3900," Phys. Fluids **36**(8), 085165 (2024).
[45]A. G. Kravchenko and P. Moin, "Numerical studies of flow over a circular cylinder at $Re_D = 3900$," Phys. Fluids **12**(2), 403–417 (2000).